Supporting Information

Engineering geometric metamorphosis in {$P_6M_2Mo_{16}O_{73}$}-based high-nuclearity metal superclusters: from tetrahedral to square assemblies via topological transformations

Xiaoyan Zhang, Hui Li, Na Xu,* Xiaodong Liu and Xiu-Li Wang*

College of Chemistry and Materials Engineering, Bohai University, Liaoning Professional Technology Innovation Center of Liaoning Province for Conversion Materials of Solar Cell, Jinzhou 121013, P. R. China

*Corresponding Authors: xun872@bhu.edu.cn; wangxiuli@bhu.edu.cn

Table of contents

Experimental Procedures

1.1 General Characterizations

Powder X-ray diffraction (PXRD) patterns of the samples were measured using a D/teX Ultra diffractometer. Fourier transform infrared spectra (FT-IR) were conducted on a Varian 640 FT-IR spectrophotometer using KBr pellets in the range of 4000–500 cm^{-1}. Scanning electron microscope images (SEM) and energy-dispersive spectroscopy (EDS) were conducted on a cold field-emission scanning electron microscope (S-4800). X-ray photoelectron spectrum (XPS) was measured using a Thermomo Scientific K-Alpha photoelectron spectrometer. The Raman spectroscopy was measured using a high-resolution confocal micro Raman spectrometer.

1.2 Synthesis of Heterometallic Molecule Clusters

1.2.1 Synthesis of $(H\mathbf{L})_{15}[(H_2P_2Mo^{V}_{2}O_9)_4(H_6P_2Co_2Mo^{V}_{4}O_{16})_2(H_4Sr\subset P_6Co_2Mo^{V}_{2}Mo^{VI}_{14}O_{73})_4]\cdot$*ca.*$142H_2O$ ($\mathbf{Co_{12}Sr_4Mo_{80}P_{36}}$**, 1**)

A mixture of $Na_2MoO_4\cdot 2H_2O$ (0.500g, 2.067 mmol), $CoCl_2\cdot 6H_2O$ (0.200 g, 0.841 mmol), $SrCl_2\cdot 6H_2O$ (0.100 g, 0.375 mmol), H_3PO_4 (0.54 ml, 10 mmol), benzimidazole (0.118 g, 1 mmol) was dissolved in a mixed solution of EtOH/H_2O (6 mL, v:v = 1:5). After being stirred for 2 h at room temperature and then the pH value was adjusted to about 1.90 with 1 M HCl and 1 M NaOH solution. Then the above mixture was placed into a 25 ml Teflon reactor and heated at 160 °C for 4 days, finally cooled to room temperature. The dark blue crystals of **1** were isolated. Yield: ~ 17.61% based on Mo. IR (KBr pellet, cm^{-1}): 3527(m), 3130(m), 2970(w), 2864(w), 2360(w), 1618(s), 1535(w), 1501(w), 1450(s), 1376(w), 1236(w), 1107(m), 1047(s), 944(s), 813(s), 748(m), 620(m), 572(m) ，482(m).

1.2.1 Synthesis of $(H\mathbf{L})_{18}[P_2Mo^{V}_{2}O_9]_2[P_{10}Ni_{4.5}Mo^{V}_{8}O_{51}]_2[NaPNiMo^{V}\mathbf{L}_{0.5}O_9]_4[Sr\subset P_6Ni_2Mo^{V}Mo^{VI}_{15}O_{73})]_2[Sr\subset P_6Ni_3Mo^{V}Mo^{VI}_{15}O_{75})]_2\cdot$*ca.*$90H_2O\cdot 2C_2H_5OH$ ($\mathbf{Na_4Ni_{23}Sr_4Mo_{88}P_{52}}$**, 2**)

The synthetic method of cluster **2** was similar to cluster **1**, except that $NiSO_4\cdot 6H_2O$ (0.200 g, 0.763mmol) was used instead of $CoCl_2\cdot 6H_2O$ (0.200 g, 0.841 mmol), and the pH value was adjusted to 2.36 by using 1 M HCl and 1 M NaOH solution. The mixture was heated at 160 °C for 4 days and cooled to room temperature. Dark blue crystals of **2** were isolated. Yield: ~ 30.65% based on Mo. IR (KBr pellet, cm^{-1}): 3527(m), 3248(w), 3140(w), 2978(w), 2869(w), 2761(w), 1643(m), 1617(s), 1565(w), 1498(w), 1448(s), 1397(w), 1266(w), 1235(w), 1097(w), 1029(s), 938(s), 805(w), 749(s), 619(m), 570(m), 490(m).

1.3 X-ray Crystallography

The crystallographic data of **1**–**2** were collected on a Bruker APEX-II CCD diffractometer with graphite-monochromated Mo Kα radiation (λ = 0.71073 Å) at 296.15 K. The structure was solved with the Shel XT structure solution program using the Intrinsic Phasing solution method and by using Olex 2 as the graphical interface.[1] The model was refined with the version of ShelXL using Least Squares minimization.[2,3] Solvent molecules with severe disorder were subjected to Solvent Mask using the Olex2 software program. The crystallographic data have been deposited with the Cambridge Crystallographic Data Centre (CCDC) as entries 2323884 and 2323886. All non-hydrogen atoms were refined anisotropically. Hydrogen atom positions were calculated geometrically and refined using the riding model.

1.4 Density Functional Theory (DFT) Calculation

DFT calculations were performed with the Gaussian16 package.[4] All optimizations were performed using M06 method, and LanL2DZ basis sets for Mo, Ni, Co and 6-31G(d,p) basis sets for other atoms in the gas phase. Vibrational frequencies were computed at the same level， and all structures were characterized with no imaginary frequencies. The figures of the Density Overlap Regions Indicator (DORI) were obtained by the Multiwfn program[5,6] and VMD soft.

1.5 The process of catalytic oxidation of methyl phenyl sulfide (MPS)

The substrate of MPS (0.5 mmol), catalyst (2.5×10^{-4} mmol), EtOH as solvent (2 mL), *tert*-butyl hydroperoxide (TBHP, 0.75 mmol, 70% aqueous), and internal standard naphthalene (20 mg) were added into the 10 mL pressure-resistant tube and agitated for 50 min under 60 °C. The conversion rate of the MPS and the selectivity of the product were analyzed using a Shimadzu Tech-comp GC-7900 gas chromatograph (GC) with a flame ionization detector equipped with a TM-5 Sil capillary column. After the reaction was completed, the catalyst was washed with EtOH and dried in the air, for subsequent reaction. Notably, a 50 mL round-bottom flask was employed as the vessel for conducting large-scale catalytic reactions.

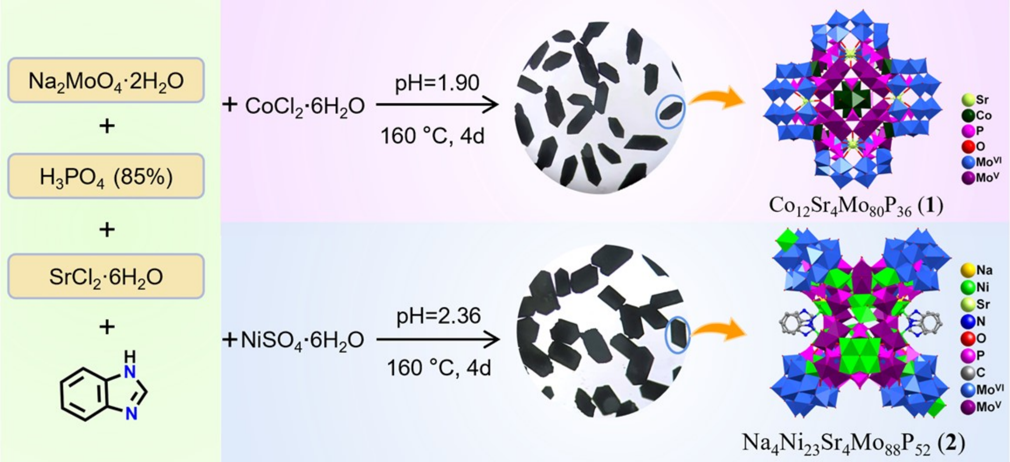

Scheme S1. The schematic diagram of the syntheses process of **$Co_{12}Sr_4Mo_{80}P_{36}$** and **$Na_4Ni_{23}Sr_4Mo_{88}P_{52}$**.

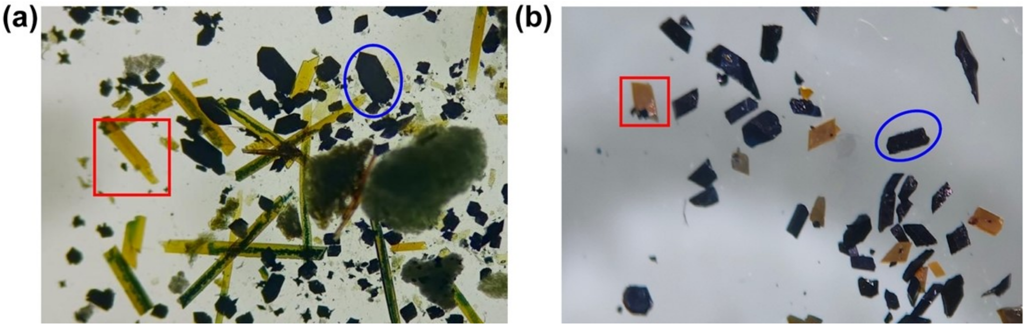

Figure S1. Optical microscopy images of the synthesized products: (a) Product from the cluster **1** synthesis reactor, with crystals of **1** highlighted by blue circles and impurity phases indicated by red boxes (Magnification information: 2.5*10); (b) Product from the cluster **2** synthesis reactor, with crystals of **2** highlighted by blue circles and impurity phases indicated by red boxes (Magnification information: 2.5*10).

During the synthesis process, we observed the formation of some impurities and other crystalline phases alongside the crystallization of the target clusters **1** and **2** (Figure S1). Specifically:

For Cluster **1**: In addition to the target cluster **1** (marked in blue circle), flocculent precipitates and yellow plate-like crystals were formed (Figure S1a). The yellow crystals were identified as a Co-containing {P_4Mo_6}-based complex structure (marked in red box).

For Cluster **2**: While a significant amount of the target cluster **2** (marked in blue circle) was obtained, a small quantity of Ni-containing {P_4Mo_6}-based complex also crystallized (marked in red box) (Figure S1b).

To ensure the purity of the target products, clusters **1** and **2** were carefully isolated through manual separation under an optical microscope. The phase purity of the selected crystals was subsequently confirmed by PXRD analysis. The experimental PXRD patterns exhibited excellent agreement with the simulated patterns, with no observable impurity phases, thereby confirming the high phase purity of the synthesized products.

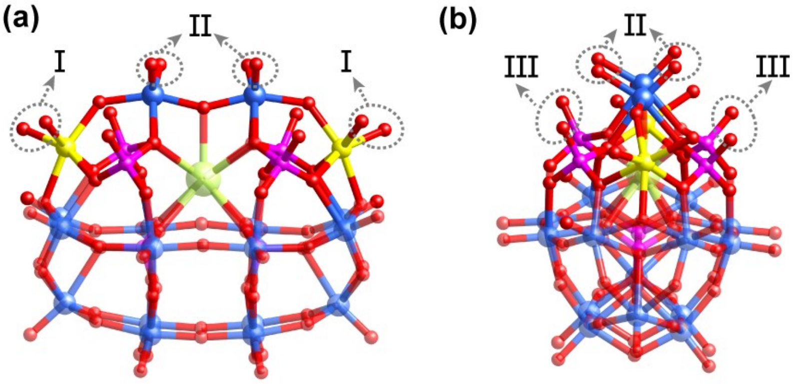

Figure S2. Three types of potential coordination sites on the handle-shaped {$P_4M_2Mo_2$} subunit within the basket-like SBUs formed by {MO_6}, {MoO_6}, and {PO_4} groups. Atoms colored blue, yellow, apple green, pink purple, and red correspond to Mo, M, Sr, P, and O, respectively.

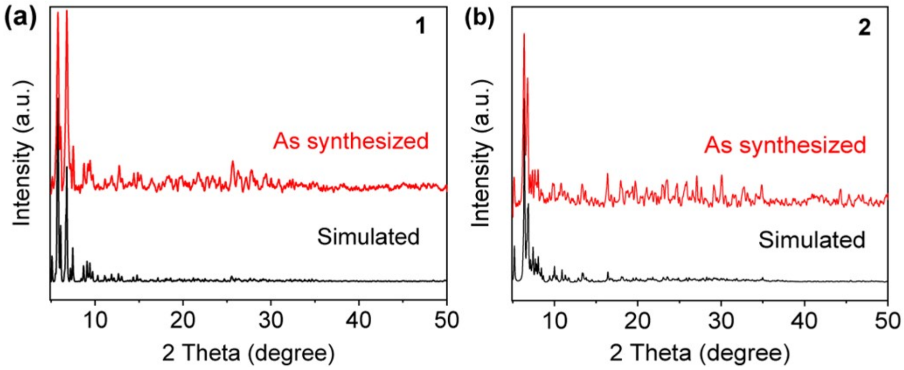

Figure S3. Simulated and experimental PXRD patterns of **1**–**2**.

The experimental and simulated PXRD patterns of **1** and **2** both show a good match, indicating high phase purity. The strength difference between the experimental PXRD pattern and the simulated PXRD pattern may be due to the change in the preferred orientation of the powder sample during the acquisition of the experimental PXRD pattern.

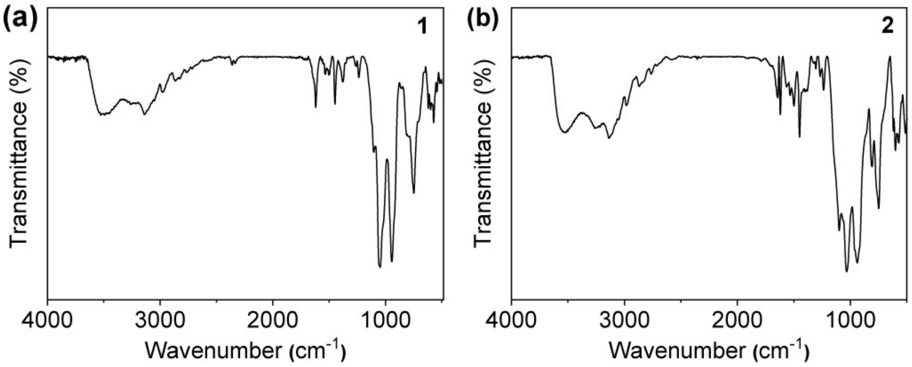

Figure S4. IR spectra of clusters **1** and **2**.

The FT-IR spectra of **1** and **2** were recorded in the range of 4000–400 cm^{-1} using KBr pellets. The strong peaks of **1**–**2** located at 3527 and 1618 cm^{-1} are assigned to *v*(O–H) stretching and bending vibrations of H_2O molecules.[7] For **1**, the peaks at 1047, 944, 813, and 748 cm^{-1} are attributed to *v*(P–O_a), *v*(Mo=$O_{terminal}$), and *v*(Mo–O_{bridge}) vibrations, respectively.[8,9] The peaks located at 620 and 572 cm^{-1} can be attributed to *v*(Mo–O–Mo).[10] The peak at 1450 cm^{-1} is attributed to *v*(C–N) vibrations.[11] For **2**, the peaks at 1029, 938, 805, and 749cm^{-1} are attributed to *v*(P–O_a), *v*(Mo=$O_{terminal}$), and *v*(Mo–O_{bridge}) vibrations, respectively.[8,9] The peaks located at 619 and 570 cm^{-1} can be attributed to *v*(Mo–O–Mo).[10] The peak at 1478 cm^{-1} is attributed to *v*(C–N) vibrations.[11]

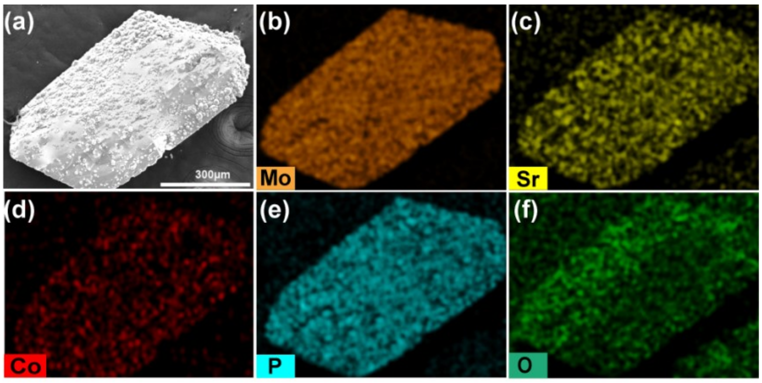

Figure S5. (a) SEM image of cluster **1**; (b–f) the element mapping of Mo, Sr, Co, P, and O elements.

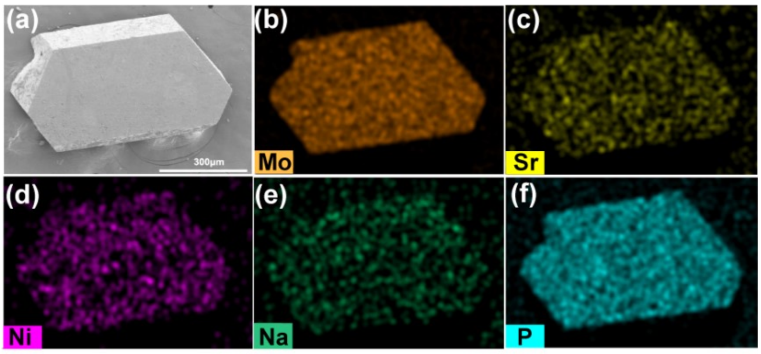

Figure S6. (a) SEM image of cluster 2; (b–f) the element mapping of Mo, Sr, Ni, Na, and P elements.

In Figures S5–S6, the high-resolution imaging technology of the SEM allows for a clear observation of the morphology of the two clusters. Notably, both clusters exhibit a very regular blocky structure. This regular block-like morphology indicates that during the growth process, the arrangement and stacking of the grains follow a certain pattern, resulting in this ordered geometric shape. Furthermore, the results from EDS analysis further demonstrate that the distribution of various elements within these two clusters is uniform.

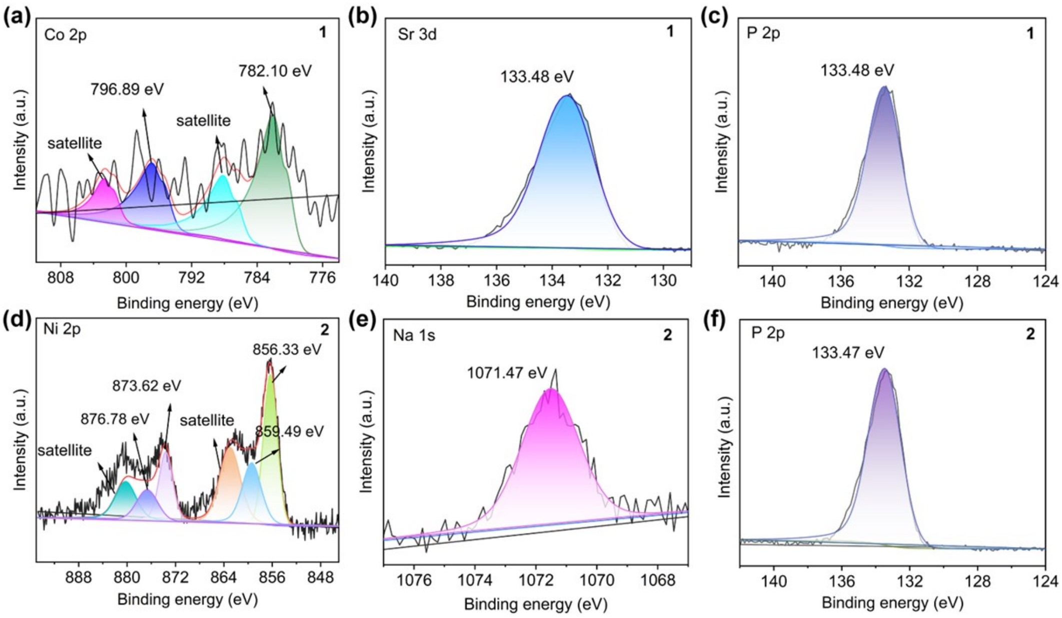

Figure S7. The XPS spectra of **1** (a) Co 2p, (b) Sr 3d, (c) P 2p. The XPS spectra of **2** (e) Ni 2p, (f) Na 1s, (g) P 2p.

The XPS studies on **1** and **2** have been systematically analyzed to elucidate the chemical states of the Mo, Co, Ni, Sr, Na, and P elements. As shown in Figure 4a, the XPS spectrum for Mo atoms displays two peaks at 233.11 and 231.61 eV in the energy region of Mo 3$d_{5/2}$, and peaks at 236.47 and 234.86 eV in the energy region of Mo 3$d_{3/2}$.[12] The peaks at 231.61 and 234.86 eV are typical for the Mo^{V} ions; whereas the Mo^{VI} ions are labeled with the characteristic peaks at 236.47 and 233.11 eV, illustrating that Mo^{VI} ions in the starting materials are partially reduced to Mo^{V} ions in the synthetic procedure. For cluster **2**, the peaks of 236.08, 234.72, 232.92, and 231.58 eV belong to Mo^{V} and Mo^{VI}, respectively (Figure 4b). The binding energies of cluster **1** at 782.10 and 796.89 eV are assigned to the Co 2$p_{3/2}$ and Co 2$p_{1/2}$ (satellite peaks at 788.22 and 802.76 eV), respectively (Figure S7a).[13] The peaks of Sr 3*d* at 133.48 eV for **1** belong to Sr^{2+} (Figure S7b).[14] For **2**, the binding energies at 856.33 and 876.78 eV were assigned to the signals of Ni 2$p_{3/2}$, while the peaks at 859.49 and 874.04 eV correspond to the Ni 2$p_{1/2}$ (satellite peaks at 863.01 and 880.31 eV), indicating the oxidation state of Ni ions was +II and +III (Figure S7d).[15] As shown in Figure S7e, the Na 1s spectrum of cluster **2** showed at 1071.47 eV, indicating the Na ions were +I.[16] The P ion acts as an anionic template and exists in both clusters in the form of {PO_4} units, playing a crucial role in the formation of these clusters. XPS analysis reveals the presence of characteristic peaks attributed to P in the +V oxidation state at 133.48 eV and 133.47 eV (Figures S7c and S7f).[17]

Supplementary Structure Description

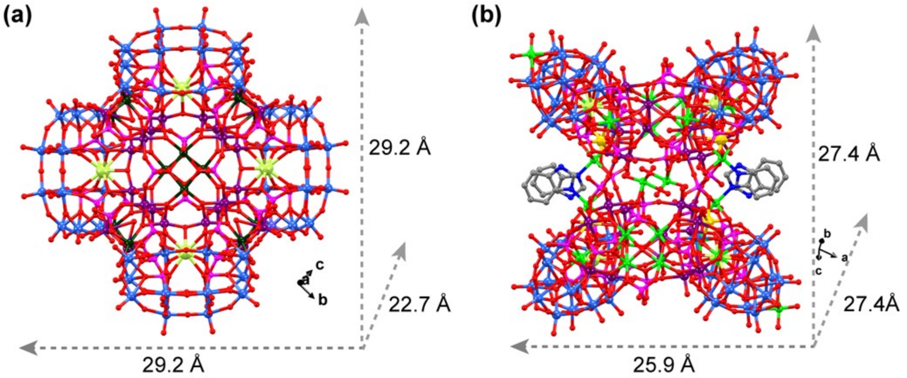

Figure S8. (a) Ball-and-stick model and the dimension of **$Co_{12}Sr_4Mo_{80}P_{36}$** established by X-ray crystallography. For clarity, the organic ligands of benzimidazole and hydrogen atoms are omitted. Atoms colored blue, deep purple, dark green, apple green, pink purple, and red correspond to Mo^{VI}, Mo^{V}, Co, Sr, P, and O, respectively. (b) Ball-and-stick model and the dimension of **$Na_4Ni_{23}Sr_4Mo_{88}P_{52}$**. The uncoordinated organic ligands of benzimidazole and hydrogen atoms are omitted for clarity. Atoms colored blue, deep purple, green, apple green, yellow, pink purple, and red correspond to Mo^{VI}, Mo^{V}, Ni, Sr, Na, P, and O, respectively.

2.1 The Crystal Structure Analysis of $Co_{12}Sr_4Mo_{80}P_{36}$

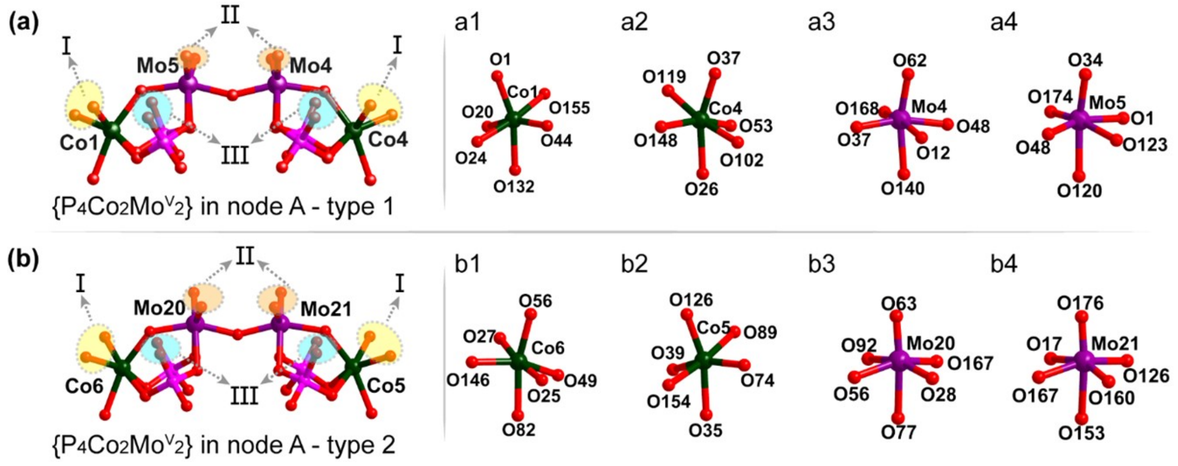

Figure S9. The coordination environment and coordination sites of the $\{P_4Co_2Mo^{V}_2\}$ subunits in the handle position of the nodes A in **$Co_{12}Sr_4Mo_{80}P_{36}$**.

In Figure S9, the $\{P_4Co_2Mo^{V}_2\}$ subunit located within node A features reactive oxygen atoms (I、II、III) on its surface that act as the aggregation points for the assembly of the cluster (Figures S9a–S9b). Within node A, the Co and Mo ions are arranged in a *hexa*-coordinate octahedral configuration (Figures S9a1–a4, S9b1–b4). The interconnection between these ions is facilitated by the sharing of oxygen atoms. The terminal oxygen atoms in this subunit connect with different linking units *via* oxygen-sharing, thereby forming a molecular cluster.

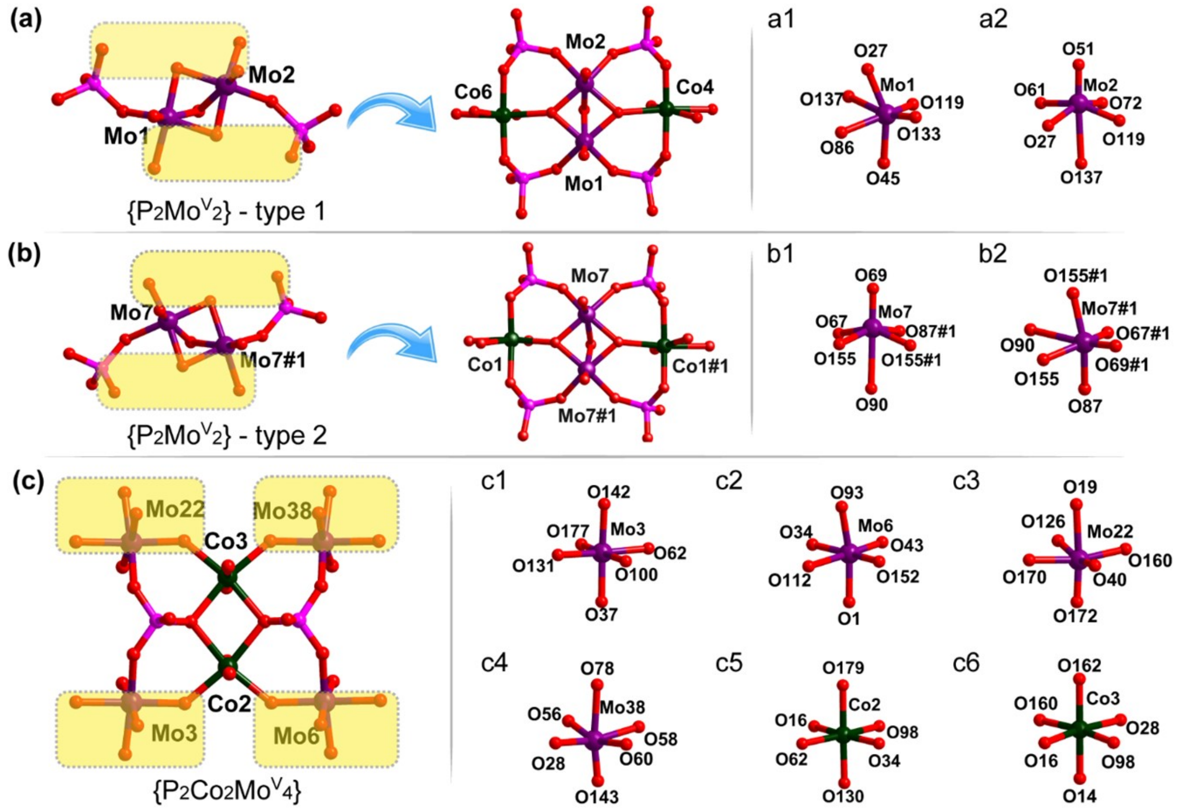

Figure S10 The coordination environment and coordination sites of the $\{P_2Mo^{V}_{2}\}$ (a–b) and $\{P_2Co_2Mo^{V}_{4}\}$ SBUs (c) within **$Co_{12}Sr_4Mo_{80}P_{36}$**.

The *trans*-configured $\{P_2Mo^{V}_{2}\}$ SBU, functioning as linker A, facilitates the formation of a dimer by bridging two node A SBUs. Specifically, the $\{P_2Mo^{V}\}$ unit connects with the Co^{II} ions and $\{PO_4\}$ groups in the $\{P_4Co_2Mo^{V}_{2}\}$ subunit at the handle position of node A through the sharing of oxygen atoms. Notably, in this process, a rectangular $\{P_4Co_2Mo^{V}_{2}\}$ unit distinct from the handle position of node A is formed (Figures S10a–S10b). In contrast to linker A, the $\{P_2Co_2Mo^{V}_{4}\}$ SBU, serving as linker B, establishes its connection with node A primarily through Mo^{V} ions. The terminal oxygen atoms of these Mo^{V} ions bond with the Mo^{V} ions in the $\{P_4Co_2Mo^{V}_{2}\}$ subunit at the handle position of node A, forming dinuclear $\{Mo^{V}_{2}\}$ units (Figure S10c). Within the $\{P_4Co_2Mo^{V}_{2}\}$ SBU, each metal ion exhibits a *hexa*-coordinate configuration (Figures S10c1–c6).

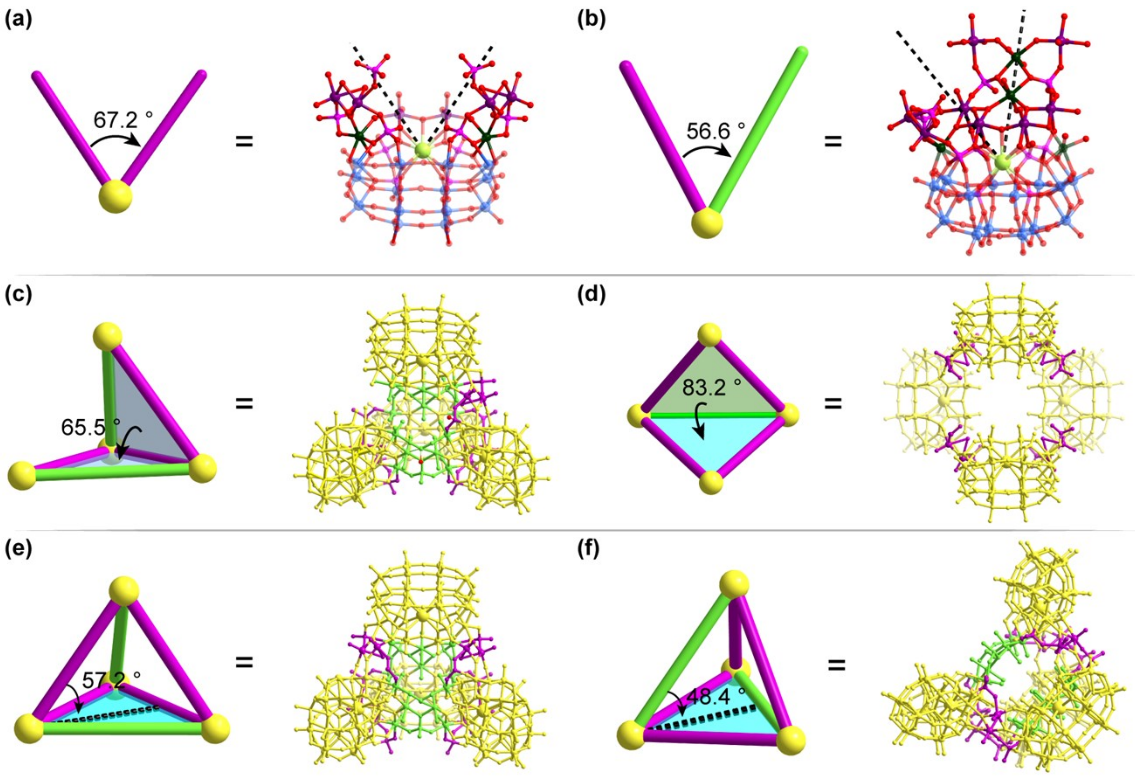

Figure S11. The relationship between linkers and nodes in **$Co_{12}Sr_4Mo_{80}P_{36}$**. (a) the angle between two linker A and one node A; (b) the angle formed between linker A and linker B with node A; (c) the dihedral angle formed by two planes intersecting through linker A; (d) the dihedral angle formed by two planes intersecting through linker B; (e) the angle between linker A and the plane containing three node A; (f) the angle between linker B and the plane containing three node A.

2.2 The Crystal Structure Analysis of $Na_4Ni_{23}Sr_4Mo_{88}P_{52}$

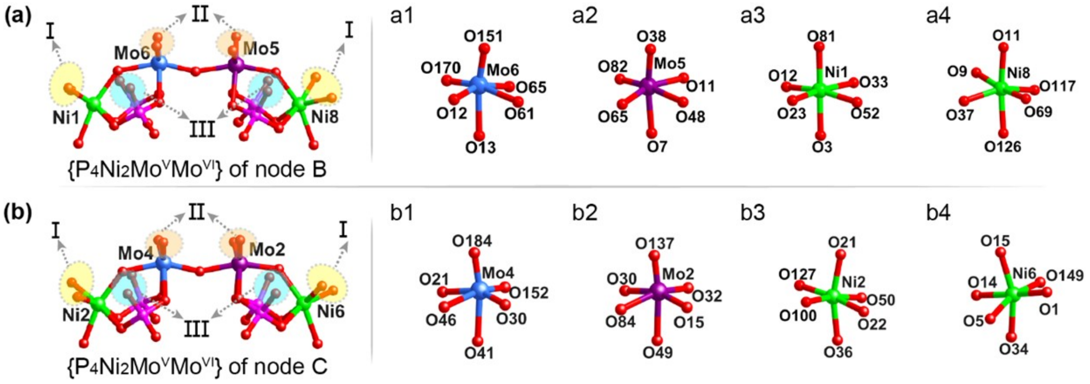

Figure S12. The coordination environment and coordination sites of the $\{P_4Ni_2Mo^VMo^{VI}\}$ subunits in the handle position of nodes B and C in **$Na_4Ni_{23}Sr_4Mo_{88}P_{52}$**.

Unlike in **$Co_{12}Sr_4Mo_{80}P_{36}$**, in **$Na_4Ni_{23}Sr_4Mo_{88}P_{52}$**, the handle positions within nodes B and C have only one Mo atom reduced to Mo^V to form the $\{P_4Ni_2Mo^VMo^{VI}\}$ subunit, leading to a change in the connection mode (Figures S12a–S12b). The subunits also serve as aggregation points for cluster formation, sharing oxygen atoms with three different linker units, thereby fully utilizing the reactive oxygen on its surface to promote the formation of macromolecular clusters. The Ni and Mo ions of the {$P_4Ni_2Mo^VMo^{VI}$} are organized in an octahedral structural arrangement.

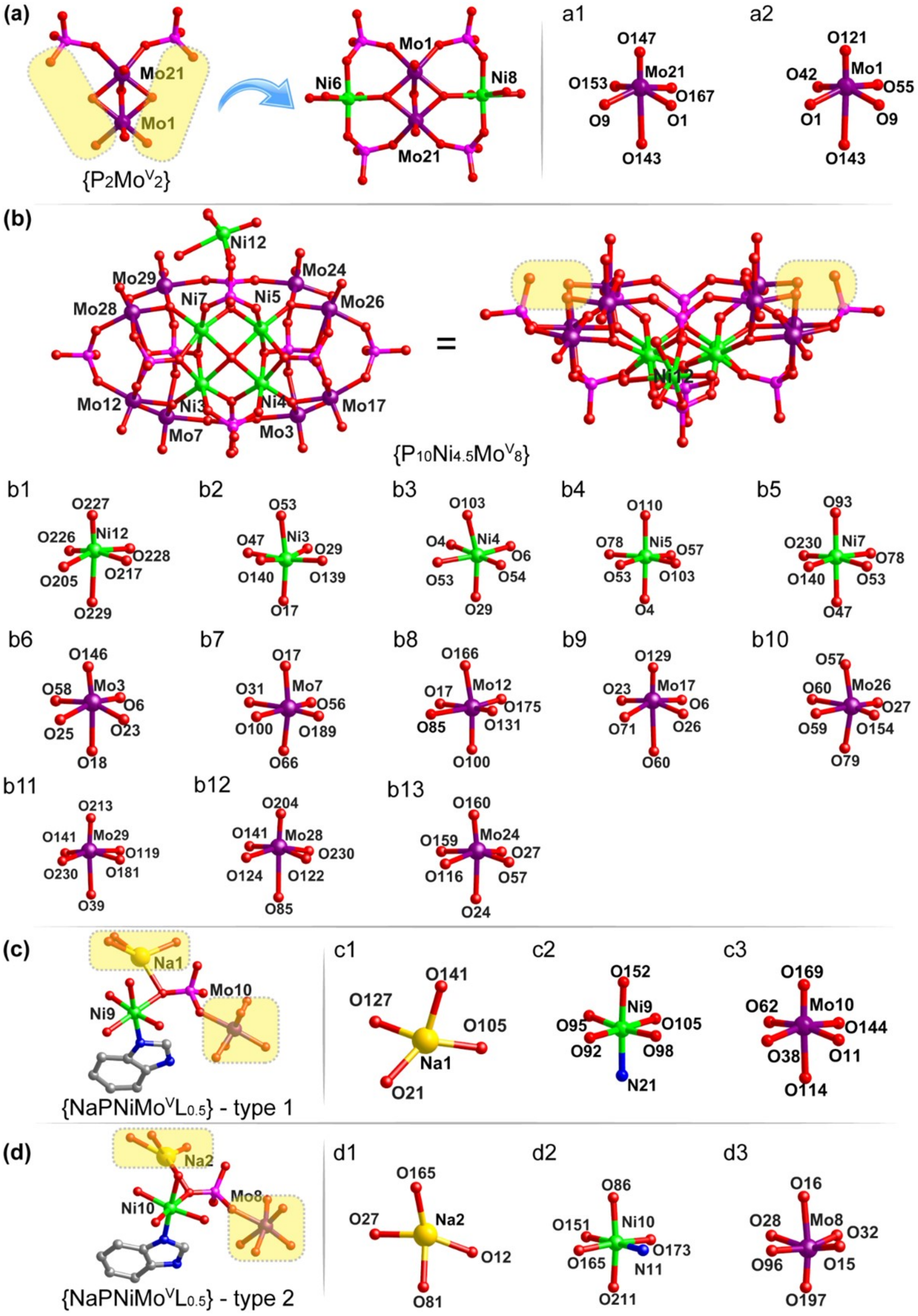

Figure S13. The coordination environment of the three connecting units: (a) the *cis*-configurated {$P_2Mo^V_2$} SBUs; (b) {$P_{10}Ni_{4.5}Mo^V_8$} SBUs; (c–d) the hammer-like {$NaPNiMo^V\mathbf{L}_{0.5}$} SBUs.

As shown in Figure 2e, linker C is composed of the *cis*-configurated {$P_2Mo^V_2$} SBU and the boat-shaped {$P_{10}Ni_{4.5}Mo^V_8$} SBU, which coordinate by sharing oxygen atoms with the {$P_4Ni_2Mo^VMo^{VI}$} subunit. On one hand, the {$P_2Mo^V_2$} SBU brings the two nodes closer together and connects them through active sites I and III of the {$P_4Ni_2Mo^VMo^{VI}$} subunit to form a quadrilateral {$P_4Ni_2Mo^V_2$} unit (Figures S13a). On the other hand, the relatively larger-sized polynuclear {$P_{10}Ni_{4.5}Mo^V_8$} SBU also coordinates with the nodes through active sites I and III (Figures S13b). Within the two connecting units, each Mo and Ni ions adopt *hexa*-coordinate octahedral structure. In Figure 2f, two {$NaPNiMo^V\mathbf{L}_{0.5}$} SBUs are connected to the {$P_4Ni_2Mo^VMo^{VI}$} subunits in nodes B and C. It is important to note that the coordination directions of the two {$NaPNiMo^V\mathbf{L}_{0.5}$} units are opposite to each other in the horizontal direction. Specifically, the Mo^V ions in the {$NaPNiMo^V\mathbf{L}_{0.5}$} SBUs will share oxygen atoms with Mo^V ions (active sites II) in the nodes to form {Mo^V_2} units, while Na^I ions and Ni^{II} ions connect with the Mo^{VI} ions (active sites II) in the nodes by sharing oxygen atoms. In linker D, the Na ions are *tetra*-coordinate, and both Mo and Ni ions are in a *hexa*-coordinate mode (Figures S13c–S13d).

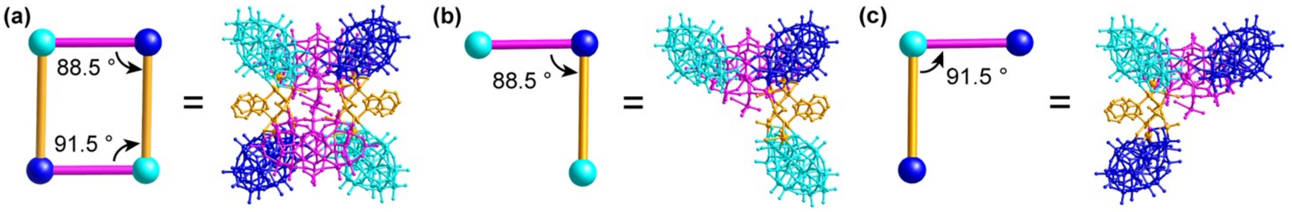

Figure S14. The relationship between linkers and nodes in $\mathbf{Na_4Ni_{23}Sr_4Mo_{88}P_{52}}$. (a) the square structure formed by connecting node B and node C to linkers C and D; (b) the angle created between linkers C and D with node B; (c) the angle developed between linkers C and D with node C.

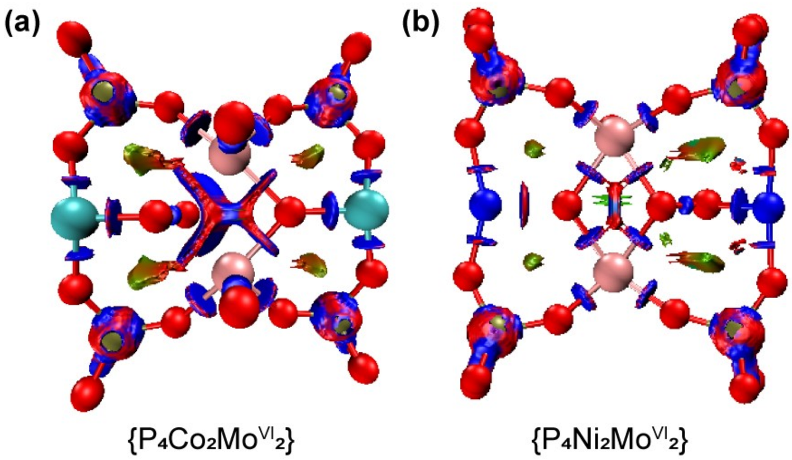

Figure S15. The DOIR of {$P_4Co_2Mo^{VI}_2$} unit and {$P_4Ni_2Mo^{VI}_2$} unit.

Supplementary Crystallographic Data Table

Table S1. Crystal data and structure refinement for **$Co_{12}Sr_4Mo_{80}P_{36}$** and **$Na_4Ni_{23}Sr_4Mo_{88}P_{52}$**.

Cluster	**$Co_{12}Sr_4Mo_{80}P_{36}$**	**$Na_4Ni_{23}Sr_4Mo_{88}P_{52}$**
Empirical formula	$C_{105}H_{105}Co_{12}Mo_{80}N_{30}O_{360}P_{36}Sr_4$	$C_{144}H_{162}Mo_{88}N_{40}Na_4Ni_{23}O_{458}P_{52}Sr_4$
Formula weight	17394.95	23230.41
Temperature/K	296.15	296.15
Crystal system	monoclinic	triclinic
Space group	*C2/c*	$P\bar{1}$
a (Å)	30.9408(19)	26.8645(19)
b (Å)	58.089(4)	27.0415(15)
c (Å)	32.2996(18)	27.3910(18)
α (Å)	90	65.064(3)
β (Å)	110.087(2)	62.244(3)
γ (Å)	90	78.094(3)
Volume(Å^3)	54522(6)	15966.1(19)
Z	4	1
D_{c} (g cm^3)	2.119	2.418
μ (mm^{-1})	2.709	2.907
F(000)	32804.0	11178.0
Reflections collected	673792	669375
Independent reflections	48156 [R_{int} = 0.0557]	62918 [R_{int} = 0.1839]
Data/restraints/parameters	48156/183/2762	62918/145/3859
GoF	1.121	1.041
R indexes [I>=2σ (I)]	R_1 [a] = 0.0588, wR_2 [b] = 0.1263	R_1 [a]= 0.0759, wR_2 [b] = 0.1553
R [all data]	R_1 [a] = 0.0633, wR_2 [b] = 0.1291	R_1 [a] = 0.1443, wR_2 [b] = 0.1972

[a] $R_1 = \Sigma||Fo|-|Fc||/\Sigma|Fo|$; [b] $wR_2 = \{\Sigma[w(Fo^2-Fc^2)^2]/\Sigma[w(Fo^2)^2]\}^{1/2}$

Table S2. The bond length (Å) in cluster **1**.

Mo1–O27	1.946(6)	Mo10–O107	2.193(6)	Mo20–O77	2.246(6)	Mo30–O118	1.883(7)	Mo40–O83	1.680(6)
Mo1–O45	2.028(6)	Mo10–O150	1.900(6)	Mo20–O92	2.159(6)	Mo30–O124	1.939(7)	Mo40–O97	1.912(6)
Mo1–O86	2.059(6)	Mo11–O11	1.682(6)	Mo20–O167	1.892(6)	Mo30–O158	2.305(7)	Mo40–O117	2.055(6)
Mo1–O119	1.964(6)	Mo11–O26	1.941(6)	Mo21–O17	2.164(6)	Mo30–O166	1.699(8)	Mo40–O125	1.892(7)
Mo1–O133	1.681(6)	Mo11–O53	2.158(6)	Mo21–O126	1.969(6)	Mo31–O3	2.086(8)	Mo40–O144	2.029(6)
Mo1–O137	2.514(7)	Mo11–O88	1.805(6)	Mo21–O153	2.257(6)	Mo31–O5	2.038(8)	Sr1–O12	2.520(6)
Mo2–O27	1.953(6)	Mo11–O164	1.824(6)	Mo21–O160	1.938(7)	Mo31–O21	1.708(8)	Sr1–O30	2.676(6)
Mo2–O51	1.666(7)	Mo11–O169	2.435(6)	Mo21–O167	1.900(6)	Mo31–O76	1.817(8)	Sr1–O32	2.701(6)
Mo2–O61	2.027(7)	Mo12–O13	1.699(6)	Mo21–O176	1.681(7)	Mo31–O101	2.414(6)	Sr1–O48	2.597(6)
Mo2–O72	2.042(6)	Mo12–O24	2.110(6)	Mo22–O19	2.274(7)	Mo31–O147	1.802(8)	Sr1–O107	2.647(6)
Mo2–O119	1.950(6)	Mo12–O80	1.839(7)	Mo22–O40^{1}	2.061(7)	Mo32–O70	1.682(8)	Sr1–O120	2.662(6)
Mo2–O137	2.472(7)	Mo12–O127	1.801(7)	Mo22–O126	1.970(7)	Mo32–O124	1.964(7)	Sr1–O123	2.523(6)
Mo3–O37	1.976(6)	Mo12–O132	2.000(6)	Mo22–O160	1.952(7)	Mo32–O147	2.070(7)	Sr1–O136	2.752(5)
Mo3–O62	1.975(5)	Mo12–O156	2.420(6)	Mo22–O170	2.105(7)	Mo32–O157	1.881(7)	Sr1–O140	2.706(5)
Mo3–O100	2.289(6)	Mo13–O23	1.820(7)	Mo22–O172	1.680(7)	Mo32–O158	2.278(7)	Sr2–O17	2.675(6)
Mo3–O131	2.104(6)	Mo13–O80	2.030(7)	Mo23–O65	2.061(8)	Mo32–O178	1.876(7)	Sr2–O64	2.726(6)
Mo3–O142	2.071(6)	Mo13–O91	1.697(7)	Mo23–O71	2.475(9)	Mo33–O7	1.900(7)	Sr2–O77	2.510(5)
Mo3–O177	1.666(7)	Mo13–O113	1.825(7)	Mo23–O89	1.967(7)	Mo33–O79	2.073(7)	Sr2–O84	2.650(6)
Mo4–O12	2.239(5)	Mo13–O128	2.049(6)	Mo23–O89^{1}	1.945(7)	Mo33–O110	2.270(6)	Sr2–O92	2.702(6)
Mo4–O37	1.987(6)	Mo13–O156	2.430(6)	Mo23–O129^{1}	2.000(7)	Mo33–O161	1.698(7)	Sr2–O103	2.650(7)
Mo4–O48	1.906(5)	Mo14–O23	2.057(7)	Mo23–O159	1.678(8)	Mo33–O178	1.865(7)	Sr2–O108	2.738(7)
Mo4–O62	1.935(5)	Mo14–O47	2.279(6)	Mo24–O22	1.669(8)	Mo33–O181	1.945(8)	Sr2–O153	2.512(7)
Mo4–O140	2.165(6)	Mo14–O57	1.843(7)	Mo24–O38	1.908(7)	Mo34–O5	1.851(7)	Sr2–O167	2.585(6)

Mo4–O168	1.682(6)	Mo14–O94	1.667(7)	Mo24–O52	2.094(7)	Mo34–O35	2.001(8)	Co1–O1	2.058(5)
Mo5–O1	1.976(5)	Mo14–O109	1.946(7)	Mo24–O108	2.176(7)	Mo34–O52	1.777(8)	Co1–O20	2.077(6)
Mo5–O34	1.946(6)	Mo14–O134	1.911(6)	Mo24–O157	1.896(7)	Mo34–O99	1.700(8)	Co1–O24	2.165(6)
Mo5–O48	1.896(6)	Mo15–O9	1.994(6)	Mo24–O180	2.088(7)	Mo34–O101	2.373(7)	Co1–O44	1.989(6)
Mo5–O120	2.163(6)	Mo15–O46	1.870(6)	Mo25–O7	1.884(6)	Mo34–O154	2.069(6)	Co1–O132	2.165(6)
Mo5–O123	2.254(6)	Mo15–O55	1.673(7)	Mo25–O33	2.064(7)	Mo35–O41	2.025(7)	Co1–O155	2.160(6)
Mo5–O174	1.684(6)	Mo15–O57	1.898(7)	Mo25–O38	1.868(7)	Mo35–O50	1.691(7)	Co2–O16	2.166(6)
Mo6–O1	1.965(5)	Mo15–O116	2.031(7)	Mo25–O64	2.161(6)	Mo35–O75	1.884(7)	Co2–O34	2.083(6)
Mo6–O34	1.970(6)	Mo15–O171	2.294(6)	Mo25–O66	1.674(8)	Mo35–O103	2.194(7)	Co2–O62	2.090(6)
Mo6–O43	1.667(6)	Mo16–O15	1.678(6)	Mo25–O68	2.077(6)	Mo35–O138	2.055(6)	Co2–O98^{1}	2.165(6)
Mo6–O93	2.073(6)	Mo16–O96	1.848(6)	Mo26–O25	2.095(6)	Mo35–O139	1.872(7)	Co2–O130	2.053(7)
Mo6–O112	2.274(6)	Mo16–O116	1.802(7)	Mo26–O31	1.820(7)	Mo36–O59	1.682(7)	Co2–O179	2.118(8)
Mo6–O152	2.117(6)	Mo16–O149	2.022(7)	Mo26–O33	1.794(7)	Mo36–O84	2.201(7)	Co3–O14	2.045(7)
Mo7–Mo7^{1}	2.5742(15)	Mo16–O164	2.025(6)	Mo26–O54	1.694(7)	Mo36–O95	2.039(6)	Co3–O16^{1}	2.149(6)
Mo7–O67	2.041(6)	Mo16–O169	2.435(6)	Mo26–O82	1.996(7)	Mo36–O118	1.889(7)	Co3–O28	2.093(6)
Mo7–O69	1.662(6)	Mo17–O26	1.990(6)	Mo26–O114	2.425(7)	Mo36–O121	2.037(8)	Co3–O98	2.157(6)
Mo7–O87^{1}	2.012(6)	Mo17–O102	2.105(6)	Mo27–O41	1.799(7)	Mo36–O139	1.863(7)	Co3–O160	2.098(6)
Mo7–O90	2.485(8)	Mo17–O111	1.671(7)	Mo27–O49	2.160(6)	Mo37–O3	1.805(7)	Co3–O162	2.100(9)
Mo7–O155^{1}	1.952(6)	Mo17–O144	1.814(6)	Mo27–O81	1.676(7)	Mo37–O35	1.974(8)	Co4–O26	2.165(6)
Mo7–O155	1.958(6)	Mo17–O149	1.831(7)	Mo27–O82	1.958(7)	Mo37–O39	2.162(7)	Co4–O37	2.046(6)
Mo8–O6	1.805(6)	Mo17–O169	2.430(6)	Mo27–O114	2.428(7)	Mo37–O101	2.444(7)	Co4–O53	2.072(6)
Mo8–O20	2.142(6)	Mo18–O47	2.263(6)	Mo27–O151	1.800(7)	Mo37–O121	1.789(8)	Co4–O102	2.193(6)
Mo8–O85	1.685(6)	Mo18–O109	1.954(7)	Mo28–O10	1.797(8)	Mo37–O135	1.694(8)	Co4–O119	2.213(6)
Mo8–O128	1.823(6)	Mo18–O113	2.092(7)	Mo28–O31	2.038(7)	Mo38–O28	1.955(6)	Co4–O148	1.976(6)

Mo8–O132	1.954(6)	Mo18–O122	1.906(7)	Mo28–O79	1.798(8)	Mo38–O56	1.976(6)	Co5–O35	2.157(7)
Mo8–O156	2.402(6)	Mo18–O145	1.686(7)	Mo28–O114	2.418(6)	Mo38–O58	2.117(6)	Co5–O39	2.080(7)
Mo9–O6	2.056(6)	Mo18–O165	1.861(6)	Mo28–O151	2.077(8)	Mo38–O60	2.065(6)	Co5–O74	2.004(8)
Mo9–O30	2.178(6)	Mo19–O9	2.005(6)	Mo28–O175	1.681(7)	Mo38–O78	2.283(6)	Co5–O89^{1}	2.194(7)
Mo9–O73	1.693(6)	Mo19–O18	1.674(6)	Mo29–O2	1.678(8)	Mo38–O143	1.666(6)	Co5–O126	2.044(6)
Mo9–O134	1.872(6)	Mo19–O96	2.035(6)	Mo29–O10	2.065(7)	Mo39–O29	1.673(7)	Co5–O154	2.182(7)
Mo9–O141	2.035(6)	Mo19–O125	1.876(7)	Mo29–O75	1.887(7)	Mo39–O97	1.862(7)	Co6–O25	2.182(7)
Mo9–O150	1.846(6)	Mo19–O165	1.881(6)	Mo29–O104	1.891(7)	Mo39–O106	2.081(6)	Co6–O27	2.204(6)
Mo10–O8	2.049(6)	Mo19–O171	2.287(6)	Mo29–O110	2.294(6)	Mo39–O122	1.865(7)	Co6–O49	2.059(6)
Mo10–O36	1.697(6)	Mo20–O28	1.945(6)	Mo29–O181	1.940(8)	Mo39–O127	2.067(6)	Co6–O56	2.041(6)
Mo10–O46	1.901(6)	Mo20–O56	1.992(6)	Mo30–O76	2.063(7)	Mo39–O136	2.171(6)	Co6–O82	2.162(6)
Mo10–O88	1.997(6)	Mo20–O63	1.685(6)	Mo30–O104	1.847(7)	Mo40–O32	2.180(6)	Co6–O146	1.986(6)

Symmetry code:^{1}-X,+Y,3/2-Z

Table S3. The bond length (Å) in cluster **2**.

Mo1–O1	1.9731	Mo13–O36	1.967	Mo25–O113	2.0681	Mo37–O174	2.049	Ni2–O100	2.0215
Mo1–O9	1.9623	Mo13–O50	2.1297	Mo25–O118	2.2801	Mo37–O193	1.8806	Ni2–O127	2.0316
Mo1–O42	2.0525	Mo13–O63	1.8256	Mo25–O128	1.9298	Mo37–O208	1.6577	Ni3–O17	2.0462
Mo1–O55	2.0584	Mo13–O112	1.8166	Mo25–O168	1.6743	Mo38–O45	1.9101	Ni3–O29	2.0231
Mo1–O121	1.6459	Mo13–O180	1.6692	Mo26–O27	1.9374	Mo38–O80	1.8464	Ni3–O47	2.0597
Mo1–O143	2.5071	Mo14–O19	2.0646	Mo26–O57	1.938	Mo38–O109	1.9566	Ni3–O53	2.132
Mo2–O15	1.9652	Mo14–O43	1.9973	Mo26–O59	2.0557	Mo38–O113	2.0401	Ni3–O139	2.0683
Mo2–O30	1.9893	Mo14–O68	1.8724	Mo26–O60	2.4143	Mo38–O118	2.2923	Ni3–O140	2.0366
Mo2–O32	1.9465	Mo14–O72	2.1797	Mo26–O79	2.0643	Mo38–O195	1.6736	Ni4–O4	2.0528
Mo2–O49	2.2354	Mo14–O91	1.6662	Mo26–O154	1.6541	Mo39–O102	2.4123	Ni4–O6	2.0133

Mo2–O84	2.1366	Mo14–O123	1.893	Mo27–O33	2.1281	Mo39–O111	2.0209	Ni4–O29	2.0542
Mo2–O137	1.672	Mo15–O8	2.1892	Mo27–O52	1.9646	Mo39–O136	2.0577	Ni4–O53	2.1372
Mo3–O6	1.9772	Mo15–O51	1.8645	Mo27–O102	2.4123	Mo39–O158	1.7826	Ni4–O54	2.0489
Mo3–O18	2.2558	Mo15–O63	2.0012	Mo27–O133	1.7919	Mo39–O209	1.8007	Ni4–O103	2.0882
Mo3–O23	1.9512	Mo15–O83	2.046	Mo27–O136	1.8185	Mo39–O225	1.6873	Ni5–O4	2.0508
Mo3–O25	2.0877	Mo15–O101	1.913	Mo27–O198	1.6894	Mo40–O69	2.0948	Ni5–O53	2.124
Mo3–O58	2.0866	Mo15–O177	1.6765	Mo28–O85	2.402	Mo40–O126	1.9862	Ni5–O57	2.0361
Mo3–O146	1.6833	Mo16–O67	2.0405	Mo28–O122	2.0773	Mo40–O138	2.4133	Ni5–O78	2.0275
Mo4–O21	2.0441	Mo16–O75	2.1806	Mo28–O124	2.0669	Mo40–O174	1.8003	Ni5–O103	2.0554
Mo4–O30	1.8317	Mo16–O94	1.8853	Mo28–O141	1.9191	Mo40–O200	1.821	Ni5–O110	2.0224
Mo4–O41	2.2208	Mo16–O142	1.8888	Mo28–O204	1.6527	Mo40–O215	1.6887	Ni6–O1	2.0909
Mo4–O46	2.227	Mo16–O145	2.0132	Mo28–O230	1.9045	Mo41–O156	1.8661	Ni6–O5	2.0491
Mo4–O152	1.728	Mo16–O155	1.6721	Mo29–O39	2.2449	Mo41–O158	2.0931	Ni6–O14	2.1296
Mo4–O184	1.7024	Mo17–O6	1.9379	Mo29–O119[1]	2.0866	Mo41–O191	1.9642	Ni6–O15	2.0792
Mo5–O7	2.13	Mo17–O23	1.9202	Mo29–O141	1.9203	Mo41–O210	1.871	Ni6–O34	2.0965
Mo5–O11	1.9722	Mo17–O26	2.0729	Mo29–O181	2.0809	Mo41–O216	1.6605	Ni6–O149	1.9879
Mo5–O38	1.9254	Mo17–O60	2.4694	Mo29–O213	1.6728	Mo41–O224	2.2684	Ni7–O47	2.0604
Mo5–O48	2.2546	Mo17–O71	2.0387	Mo29–O230	1.9518	Mo42–O132	2.2868	Ni7–O53	2.1085
Mo5–O65	2.0036	Mo17–O129	1.68	Mo30–O70	2.0139	Mo42–O163	1.8881	Ni7–O78	2.0201
Mo5–O82	1.6761	Mo18–O5	2.1691	Mo30–O74	2.02	Mo42–O183	1.8668	Ni7–O93	2.0394
Mo6–O12	2.0493	Mo18–O34	1.9719	Mo30–O76	2.47	Mo42–O196	2.0438	Ni7–O140	2.0429
Mo6–O13	2.2198	Mo18–O43	1.8325	Mo30–O90	1.8688	Mo42–O207	1.9193	Ni7–O230	2.0628
Mo6–O61	2.2147	Mo18–O70	1.819	Mo30–O157	1.8605	Mo42–O214	1.6746	Ni8–O9	2.1084
Mo6–O65	1.8169	Mo18–O76	2.388	Mo30–O199	1.6705	Mo43–O138	2.4449	Ni8–O11	2.0096

Mo6–O151	1.7287	Mo18–O97	1.6713	Mo31–O20	2.094	Mo43–O171	2.0563	Ni8–O37	2.0614
Mo6–O170	1.6847	Mo19–O22	2.1144	Mo31–O44	2.1726	Mo43–O196	1.8137	Ni8–O69	2.1325
Mo7–O17	1.9494	Mo19–O35	2.3823	Mo31–O94	1.8679	Mo43–O200	2.0468	Ni8–O117	1.9759
Mo7–O31	2.2398	Mo19–O36	1.9948	Mo31–O130	2.0331	Mo43–O203	1.7948	Ni8–O126	2.0999
Mo7–O56	2.0787	Mo19–O88	1.8197	Mo31–O161	1.6727	Mo43–O219	1.6699	Ni9–O92	2.1009
Mo7–O66	2.0979	Mo19–O99	1.8191	Mo31–O163	1.8851	Mo44–O132	2.2955	Ni9–O95^{1}	2.0642
Mo7–O100	1.9613	Mo19–O148	1.6848	Mo32–O35	2.4185	Mo44–O193	1.8896	Ni9–O98	2.0672
Mo7–O189	1.6556	Mo20–O77	2.2994	Mo32–O99	2.0056	Mo44–O203	2.0638	Ni9–O105	2.0581
Mo8–O15	1.9602	Mo20–O104	2.062	Mo32–O107	1.8624	Mo44–O207	1.9569	Ni9–O152^{1}	2.0609
Mo8–O16	2.2199	Mo20–O106	1.8629	Mo32–O109	1.8659	Mo44–O210	1.8657	Ni9–N21	2.0546
Mo8–O28^{1}	2.0875	Mo20–O128	1.9034	Mo32–O112	2.0113	Mo44–O212	1.6847	Ni10–O86	2.0686
Mo8–O32	1.9464	Mo20–O157	1.9701	Mo32–O186	1.6547	Sr1–O8	2.6523	Ni10–O151	2.076
Mo8–O96	2.105	Mo20–O185	1.6884	Mo33–O40	2.18	Sr1–O10	2.7178	Ni10–O165	2.0745
Mo8–O197	1.6728	Mo21–O1	1.9627	Mo33–O108	2.0726	Sr1–O30	2.6889	Ni10–O173	2.0925
Mo9–O2	2.0768	Mo21–O9	1.9455	Mo33–O133	2.0364	Sr1–O41	2.5792	Ni10–O211	2.0772
Mo9–O10	2.186	Mo21–O143	2.5077	Mo33–O135	1.8829	Sr1–O46	2.6867	Ni10–N11	2.0408
Mo9–O51	1.8919	Mo21–O147	1.6477	Mo33–O156	1.9054	Sr1–O49	2.5653	Ni11–O45	2.278
Mo9–O89	2.0232	Mo21–O153	2.0454	Mo33–O182	1.6729	Sr1–O72	2.6067	Ni11–O104	2.0366
Mo9–O106	1.9025	Mo21–O167	2.0455	Mo34–O45	1.9254	Sr1–O84	2.778	Ni11–O113	2.002
Mo9–O194	1.6713	Mo22–O14	2.0993	Mo34–O77	2.3108	Sr1–O87	2.6323	Ni11–O128	2.38
Mo10–O11	1.9456	Mo22–O34	1.975	Mo34–O90	1.941	Sr2–O7	2.7563	Ni11–O218	1.655
Mo10–O38	1.9395	Mo22–O74	1.828	Mo34–O104	2.0536	Sr2–O13	2.6796	Ni11–O220	1.6696
Mo10–O62	2.0733	Mo22–O76	2.3883	Mo34–O123	1.8645	Sr2–O40	2.6695	Ni12–O205	2.0988
Mo10–O114	2.2195	Mo22–O89	1.813	Mo34–O176	1.6804	Sr2–O44	2.6095	Ni12–O217	2.0448

Mo10–O144	2.1002	Mo22–O201	1.6875	Mo35–O37	2.1497	Sr2–O48	2.5343	Ni12–O226	1.697
Mo10–O169	1.6785	Mo23–O3	2.1286	Mo35–O126	1.9687	Sr2–O61	2.5607	Ni12–O227	1.759
Mo11–O68	1.8793	Mo23–O52	1.9927	Mo35–O130	1.8002	Sr2–O64	2.7369	Ni12–O228	1.9739
Mo11–O73	2.0409	Mo23–O102	2.3845	Mo35–O138	2.4008	Sr2–O65	2.7034	Ni12–O229	2.4743
Mo11–O80	1.923	Mo23–O111	1.8557	Mo35–O171	1.805	Sr2–O75	2.6227	Na1–O21	2.3662
Mo11–O87	2.1819	Mo23–O145	1.7936	Mo35–O206	1.6815	Ni1–O3	2.0763	Na1–O105[1]	2.3004
Mo11–O88	1.9959	Mo23–O179	1.6657	Mo36–O142	1.883	Ni1–O12	2.013	Na1–O127	2.3273
Mo11–O162	1.6961	Mo24–O24	2.2319	Mo36–O183	1.8603	Ni1–O23	2.0215	Na1–O141	2.3319
Mo12–O17	1.9522	Mo24–O27	1.935	Mo36–O188	1.6988	Ni1–O33	2.0955	Na2–O12	2.3655
Mo12–O85	2.4687	Mo24–O57	1.9638	Mo36–O191	1.9425	Ni1–O52	2.0572	Na2–O27	2.3232
Mo12–O100	1.9326	Mo24–O116	2.0818	Mo36–O209	2.0684	Ni1–O81	2.031	Na2–O81	2.3333
Mo12–O131	2.0259	Mo24–O159	2.0638	Mo36–O224	2.2877	Ni2–O21	2.0177	Na2–O165	2.3179
Mo12–O166	2.0369	Mo24–O160	1.6745	Mo37–O64	2.1642	Ni2–O22	2.0863		
Mo12–O175	1.666	Mo25–O101	1.8603	Mo37–O115	2.0701	Ni2–O36	2.0573		
Mo13–O35	2.4276	Mo25–O107	1.9557	Mo37–O135	1.8703	Ni2–O50	2.1045		

Symmetry code:[1]1-X,1-Y,1-Z

Table S4. BVS values for Mo, Sr, and Co atoms in cluster **1**.

Atom	BVS	Atom	BVS	Atom	BVS	Atom	BVS	Atom	BVS	Atom	BVS
Mo1	5.177	Mo9	5.918	Mo17	6.039	Mo25	5.841	Mo33	5.814	Co1	1.975
Mo2	5.323	Mo10	5.726	Mo18	5.823	Mo26	6.035	Mo34	6.039	Co2	1.900
Mo3	5.165	Mo11	6.065	Mo19	5.872	Mo27	6.161	Mo35	5.815	Co3	1.928
Mo4	5.477	Mo12	5.893	Mo20	5.466	Mo28	6.117	Mo36	5.868	Co4	1.950
Mo5	5.480	Mo13	5.915	Mo21	5.513	Mo29	5.877	Mo37	6.041	Co5	1.937
Mo6	5.185	Mo14	6.024	Mo22	5.187	Mo30	5.904	Mo38	5.206	Co6	1.971

Mo7	5.352	Mo15	5.869	Mo23	5.262	Mo31	5.888	Mo39	5.900	Sr1	2.226
Mo8	6.069	Mo16	6.059	Mo24	5.629	Mo32	5.864	Mo40	5.745	Sr2	2.258

Table S5. BVS values for Mo, Sr, Ni, and Na atoms in cluster **2**.

Atom	BVS	Atom	BVS	Atom	BVS	Atom	BVS	Atom	BVS	Atom	BVS
Mo1	5.259	Mo11	5.762	Mo21	5.350	Mo31	5.858	Mo41	6.004	Ni5	2.141
Mo2	5.390	Mo12	5.385	Mo22	6.036	Mo32	5.995	Mo42	6.058	Ni6	2.038
Mo3	5.164	Mo13	6.067	Mo23	6.045	Mo33	5.777	Mo43	6.126	Ni7	2.121
Mo4	6.126	Mo14	5.969	Mo24	5.353	Mo34	5.839	Mo44	5.868	Ni8	2.089
Mo5	5.365	Mo15	5.899	Mo25	5.839	Mo35	6.120	Sr1	2.132	Ni9	2.050
Mo6	6.264	Mo16	5.923	Mo26	5.398	Mo36	5.869	Sr2	2.163	Ni10	2.028
Mo7	5.360	Mo17	5.290	Mo27	6.097	Mo37	5.964	Ni1	2.161	Ni11	3.162
Mo8	5.277	Mo18	5.986	Mo28	5.506	Mo38	5.974	Ni2	2.139	Ni12	2.946
Mo9	5.778	Mo19	5.994	Mo29	5.376	Mo39	6.199	Ni3	2.095	Na1	0.961
Mo10	5.332	Mo20	5.789	Mo30	5.842	Mo40	6.064	Ni4	2.070	Na2	0.950

Supplementary MPS Catalytic Performance

Table S6. Conversion and selectivity of the oxidation of MPS to MPSO by **$Na_4Ni_{23}Sr_4Mo_{88}P_{52}$** with TBHP as the oxidant. [a]

Entry	Cat. (μmol)	Solvent	TBHP (mmol)	Temp. (°C)	Conv. [b] (%)	Sel. [c] (%)
1	0.25	CH_3CN	0.75	60	42.8	98.7
2	0.25	MeOH	0.75	60	95.9	98.5
3	**0.25**	**EtOH**	**0.75**	**60**	**99.5**	**98.9**
4	0.25	Diox	0.75	60	57.1	98.6
5	0.15	EtOH	0.75	60	99.7	94.0
6	0.20	EtOH	0.75	60	99.4	98.5
7	0.30	EtOH	0.75	60	99.7	97.3
8	0.25	EtOH	0.60	60	96.2	99.0
9	0.25	EtOH	0.65	60	97.7	98.3
10	0.25	EtOH	0.70	60	99.4	97.1
11	0.25	EtOH	0.80	60	99.4	98.2
12	0.25	EtOH	0.75	40	89.0	99.1
13	0.25	EtOH	0.75	50	98.1	98.4
14	0.25	EtOH	0.75	70	99.6	92.9
15	2.50	EtOH	7.50	60	99.2	95.5

[a] Reaction conditions: 0.5 mmol of MPS, 50 min. [b] Conversion and selectivity were determined by GC using naphthalene as an internal standard, [c] Selectivity to MPSO, the byproduct of which was sulfone.

Table S7. Comparison of POM-based crystalline heterogeneous catalytic systems for MPS oxidation.

Catalyst	Oxidant	Time (min)	Tem. (℃)	Conv. (%)	Sel. of MPSO (%)	Ref.
$Co_{12}Sr_4Mo_{80}P_{36}$	TBHP	50	60	99.3	97.6	This work
$Na_4Ni_{23}Sr_4Mo_{88}P_{52}$	TBHP	50	60	99.5	98.9	This work
Ni_2V_4 Cu_2V_4 CuV_2	H_2O_2	240	45	98.6 98.8 91.5	98.7 96.5 98.5	18
$Zr_{24}Ge_6W_{56}$	H_2O_2	60	60	99	16	19
$Cu_3Co_2Mo_{10}$ $Cu_5Co_4Mo_{20}$ $Na_2CuCo_4Mo_{20}$	TBHP	240	40	99.0 94.8 96.7	100.0 95.1 96.3	20
Zn_4PMo_{12}	H_2O_2	10	50	>99	>99	21
$Co_4Se_8V_{20}$	TBHP	60	25	98.9	100	22
Cu_6PW_{12}	TBHP	50	50	>99	99.0	23
$NiMo_2$ $CuMo_8$ Ni_2CrMo_6	TBHP	40	50	99.5 99.2 99.0	98.6 98.1 97.3	24
$Ru_2As_4W_{40}$	H_2O_2	50	60	97.4	87	25

MnV_{10}	H_2O_2	240	50	97.5	98.5	26
$Mn_3Se_8V_{20}$ $Co_3Se_8V_{20}$	TBHP	60	25	96.2 98.8	97.8 97.9	27
$CuBW_{12}$	H_2O_2	70	45	98.2	94.6	28
Cu_2Mo_{16}	H_2O_2	45	R.t.	96	98	29
$Na_{14}Co_4PW_9$	H_2O_2	110	R.t.	99	75	30
Cu_2Mo_8	H_2O_2	60	40	99	99	31
CoV_2	TBHP	15	50	98	98	32
$NaRu_6AsW_{72}$	H_2O_2	60	40	95.1	99	33
$Cu_2(CrMo_6)_3$	TBHP	30	50	99	99	34
$CuTeMo_6$	TBHP	60	30	57	100	35

Table S8. Selective oxidation of various sulfides to sulfoxides. [a]

Entry	Substrates	Products	Conv. [b] (%)	Sel. [b] (%)
1	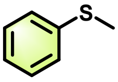	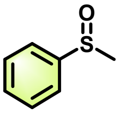	99.5	98.9
2	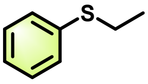	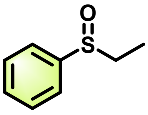	99.4	96.5
3	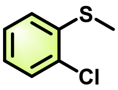	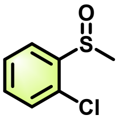	91.1	96.6
4	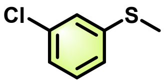	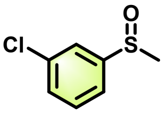	97.6	97.1
5	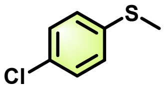	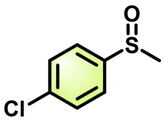	98.4	99.6
6	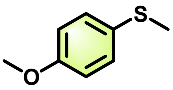	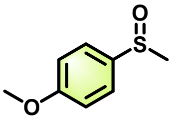	99.1	96.2
7	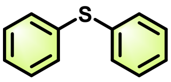	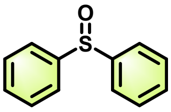	93.9	97.4

8	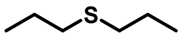	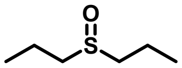	99.2	92.2
9	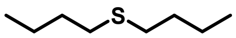	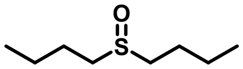	99.7	95.6

[a] Reaction conditions: 0.25 μmol of **2**, 0.5 mmol of substrates, 2 mL EtOH, 0.75 mmol 70% TBHP, 60 °C, 50 min. [b] Conversion and selectivity were determined by GC using naphthalene as an internal standard.

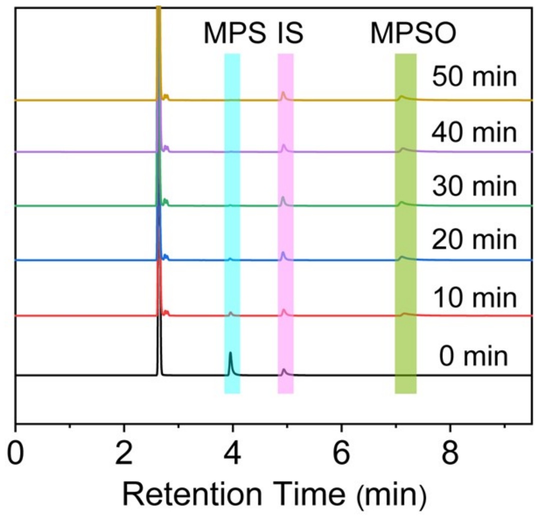

Figure S16. The GC-FID signals of the catalytic oxidation of MPS reaction after a 10-fold scale-up (IS = internal standard).

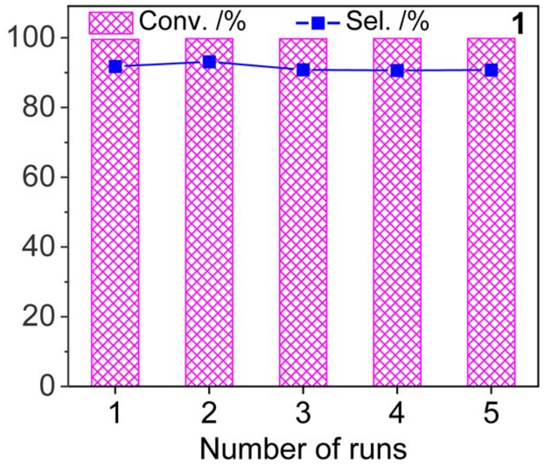

Figure S17. The cyclic experiment of cluster **1**.

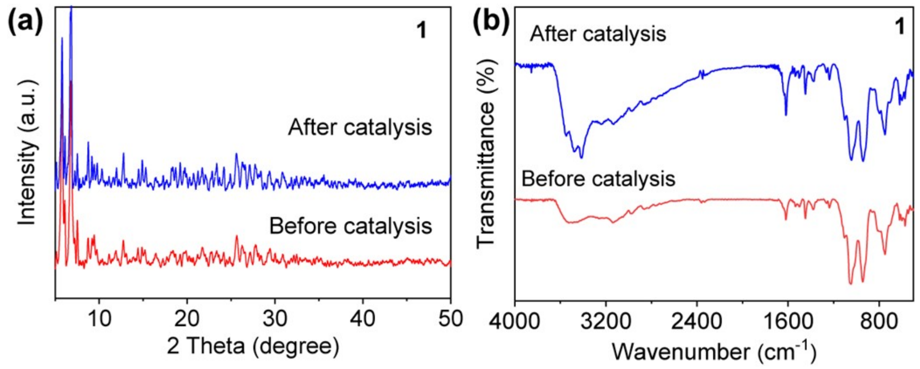

Figure S18. (a) The PXRD patterns of **1** before and after the catalysis; (b) IR spectra of **1** before and after the catalysis.

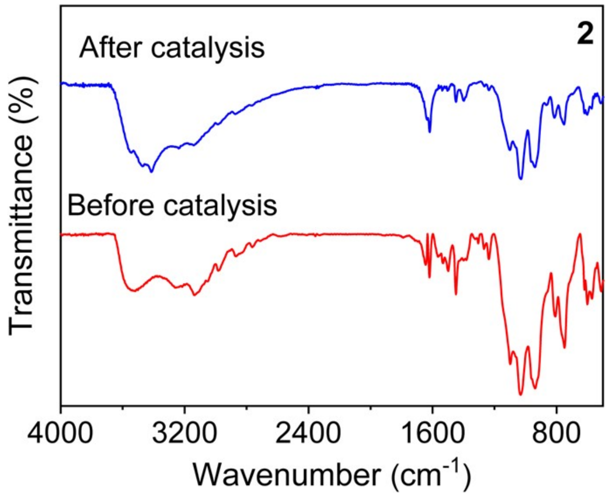

Figure S19. IR spectra of **2** before and after the catalytic reaction.

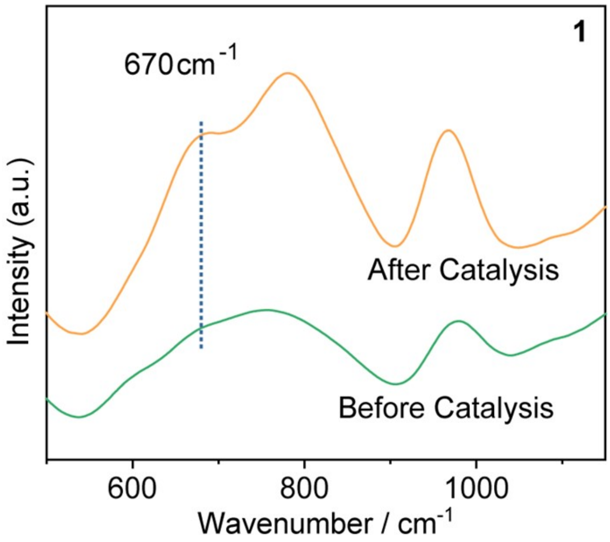

Figure S20. The Raman spectra of **1** before and after the catalytic reaction.

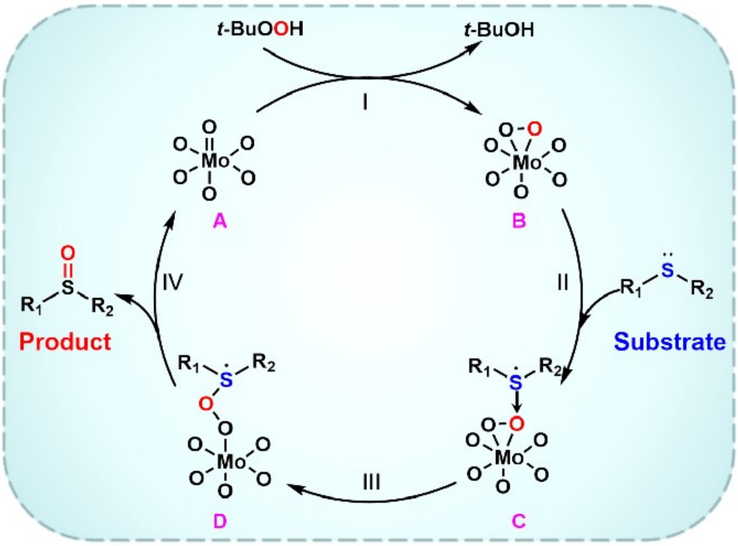

Figure S21. The possible mechanism of sulfide catalytic oxidation.

References

1 G. M. Sheldrick, A short history of SHELX, *Acta Cryst.*, 2007, **64**, 112–122.

2 A. L. Spek, Structure validation in chemical crystallography, *Acta Crystallogr. Sect. D Biol. Crystallogr.*, 2009, **65**, 148-155.

3 G. M. Sheldrick, SHELXT – Integrated space-group and crystal-structure determination, *Acta Cryst.* , 2015, **71**, 3–8.

4 M. Frisch and F. Clemente, MJ Frisch, GW Trucks, HB Schlegel, GE Scuseria, MA Robb, JR Cheeseman, G, *Scalmani, V. Barone, B. Mennucci, GA Petersson, H. Nakatsuji, M. Caricato, X. Li, HP Hratchian, AF Izmaylov, J. Bloino and G. Zhe, Gaussian*, **9**.

5 T. Lu and F. Chen, Multiwfn: A multifunctional wavefunction analyzer, *J. Comput. Chem.*, 2011, **33**, 580–592.

6 T. Lu, A comprehensive electron wavefunction analysis toolbox for chemists, Multiwfn, *J. Chem. Phys.*, 2024, **161**, *082503.*

7 B. Z. Lin, G. H. Han, B. H. Xu, L. Bai, Y. L. Feng and H. Su, Hydrothermal Synthesis and Characterization of Two New Phosphatomolybdates(V) Containing Sandwich-Shaped [M(Mo_6P_4)$_2$] Clusters (M = Co, Ni), *J. Cluster Sci.*, 2008, **19**, 379–390.

8 X. Xin, X. Tian, H. Yu and Z. Han, Synthesis of Hybrid Phosphomolybdates and Application as Highly Stable and Effective Catalyst for the Reduction of Cr(VI), *Inorg. Chem.*, 2018, **57**, 11474–11481.

9 K. Gong, Y. Liu and Z. Han, Manganese-phosphomolybdate molecular catalysts for the electron transfer reaction of ferricyanide to ferrocyanide, *RSC Adv.*, 2015, **5**, 47004–47009.

10 X. Zhang, N. Xu, X. Liu, Y. Guo, Z. Shang and X. Wang, Scalable synthesis of a new {$P_2Mo_{18}O_{62}$}-modified Cu^I/Cu^{II}-based metal–organic complex for multi-center synergistic catalysis of benzyl alcohol to benzoic acid, *Molecular Catalysis*, 2024, **568**, 114478.

11 X. Liu, L. Zhang, J. Wang, N. Xu, X. Zhang, Z. Chang and X. Wang, Two $\{Cu^{I}[P_4Mo_6]^{2}\}$-Based Coordination Polymers Incorporating In Situ Converted Tetrapyridyl Ligands for Trace Analysis of Nitrofuran Antibiotics, *Inorg. Chem.*, 2024, **63**, 9058–9065.

12 J. S. Qin, D. Y. Du, W. Guan, X. J. Bo, Y. F. Li, L. P. Guo, Z. M. Su, Y. Y. Wang, Y. Q. Lan and H. C. Zhou, Ultrastable Polymolybdate-Based Metal–Organic Frameworks as Highly Active Electrocatalysts for Hydrogen Generation from Water, *J. Am. Chem. Soc.*, 2015, **137**, 7169–7177.

13 B. J. Tan, K. J. Klabunde and P. A. Sherwood, XPS Studies of Solvated Metal Atom Dispersed Catalysts. Evidence for Layered Cobalt-Manganese Particles on Alumina and Silica, *J. Am. Chem. Soc.*, 1991, **13**, 855–861.

14 S. Komai, M. Hirano and N. Ohtsu, Spectral analysis of Sr 3d XPS spectrum in Sr-containing hydroxyapatite, *Surf. Interface Anal.*, 2020, **52**, 823–828.

15 Z. Fu, J. Hu, W. Hu, S. Yang and Y. Luo, Quantitative analysis of Ni^{2+}/Ni^{3+} in $Li[Ni_xMn_yCo_z]O_2$ cathode materials: Non-linear least-squares fitting of XPS spectra, *Appl. Surf. Sci.*, 2018, **441**, 1048–1056.

16 Y. Wang, F. Liu, G. Fan, X. Qiu, J. Liu, Z. Yan, K. Zhang, F. Cheng and J. Chen, Electroless Formation of a Fluorinated Li/Na Hybrid Interphase for Robust Lithium Anodes, *J. Am. Chem. Soc.*, 2021, **143**, 2829–2837.

17 D. Liu, B. Chen, J. Li, Z. Lin, P. Li, N. Zhen, Y. Chi and C. Hu, Imidazole-Functionalized Polyoxometalate Catalysts for the Oxidation of 5-Hydroxymethylfurfural to 2,5-Diformylfuran Using Atmospheric O_2, *Inorg. Chem.*, 2021, **60**, 3909–3916.

18 J. Li, C. Wei, D. Guo, C. Wang, Y. Han, G. He, J. Zhang, X. Huang and C. Hu, Inorganic–organic hybrid polyoxovanadates based on $[V_4O_{12}]^{4-}$ or $[VO_3]_2^{2-}$ clusters: controllable synthesis, crystal structures and catalytic properties in selective oxidation of sulfides, *Dalton Trans.*, 2020, **49**, 14148–14157.

19 L. Huang, S. S. Wang, J. W. Zhao, L. Cheng and G. Y. Yang, Synergistic Combination of Multi-Zr^{IV} Cations and Lacunary Keggin Germanotungstates Leading to a Gigantic Zr_{24}-Cluster-Substituted Polyoxometalate, *J. Am. Chem. Soc.*, 2014, **136**, 7637–7642.

20 H. An, Y. Hou, L. Wang, Y. Zhang, W. Yang and S. Chang, Evans–Showell-Type Polyoxometalates Constructing High-Dimensional Inorganic–Organic Hybrid Compounds with Copper–Organic Coordination Complexes: Synthesis and Oxidation Catalysis, *Inorg. Chem.*, 2017, **56**, 11619–11632.

21 Y. Chen, H. An, S. Chang, Y. Li, Q. Zhu, H. Luo and Y. Huang, A POM-based porous supramolecular framework for efficient sulfide–sulfoxide transformations with a low molar O/S ratio, *Inorg. Chem. Front.*, 2022, **9**, 3282–3294.

22 R. Wan, P. He, Z. Liu, X. Ma, P. Ma, V. Singh, C. Zhang, J. Niu and J. Wang, A Lacunary Polyoxovanadate Precursor and Transition-Metal-Sandwiched Derivatives for Catalytic Oxidation of Sulfides, *Chem. Eur. J.*, 2020, **26**, 8760–8766.

23 Y. Chen, H. An, S. Chang, Y. Li, T. Xu, Q. Zhu, H. Luo, Y. Huang and Y. Wei, Two pseudo-polymorphic porous POM-pillared

MOFs for sulfide-sulfoxide transformation: Efficient synergistic effects of POM precursors, metal sites and microstructures, *Chin. Chem. Lett.*, 2023, **34**, 107856.

24 X. Wang, J. Lin, H. Li, C. Wang and X. Wang, Carbazole-based bis-imidazole ligand-involved synthesis of inorganic–organic hybrid polyoxometalates as electrochemical sensors for detecting bromate and efficient catalysts for selective oxidation of thioether, *RSC Advances*, 2022, **12**, 4437–4445.

25 M. Han, Y. Niu, R. Wan, Q. Xu, J. Lu, P. Ma, C. Zhang, J. Niu and J. Wang, A Crown-Shaped Ru-Substituted Arsenotungstate for Selective Oxidation of Sulfides with Hydrogen Peroxide, *Chem. Eur. J.*, 2018, **24**, 11059–11066.

26 J. K. Li, C. P. Wei, Y. Y. Wang, M. Zhang, X. R. Lv and C. W. Hu, Conversion of V_6 to V_{10} cluster: Decavanadate-based Mn-polyoxovanadate as robust heterogeneous catalyst for sulfoxidation of sulfides, *Inorg. Chem. Commun.*, 2018, **87**, 5–7.

27 R. Wan, Z. Jing, Q. Xu, X. Ma, P. Ma, C. Zhang, J. Niu and J. Wang, Lacunary $\{Se_4V_{10}\}$ Heteropolyoxovanadate Precursor with Monometal, Metal-Richer-Sandwiched Derivatives $\{Se_8V_{20}M\}$ and $\{Se_8V_{20}M_3\}$: Correlations between the Synthesis, Structure, and Catalytic Property, *Inorg. Chem.*, 2021, **60**, 2888–2892.

28 Y. Hou, P. Han, L. Zhang, H. Li and Z. Xu, pH-controlled assembling of POM-based metal–organic frameworks for use as supercapacitors and efficient oxidation catalysts for various sulfides, *Inorg. Chem. Front.*, 2023, **10**, 148–157.

29 L. Yang, Z. Zhang, C. N. Zhang and X. L. Wang, A bifunctional POM-based Cu-viologen complex with mixed octamolybdate clusters for rapid oxidation desulfurization and effective photogeneration of hydrogen, *Rare Met.*, 2023, **43**, 236–246.

30 H. Naslhajian, M. Amini, M. Amin Dastyar, A. Bayrami, M. Bagherzadeh, S. Morteza F. Farnia and J. Janczak, Selective oxidation of organosulfurs with a sandwich-type polyoxometalate/hydrogen peroxide system, *Polyhedron*, 2020, **186**, 114622.

31 X. Huang, Y. Cui, G. Liu, H. Wang, J. Ren, Y. Zhang, G. Shen, L. Lv, H.-W. Wang and Y.-F. Chen, Imidazole-Dependent Assembly of Copper Polymolybdate Frameworks for One-Pot Sulfide Oxidation and C–H Activation, *Energy Fuels*, 2022, **36**, 1665–1675.

32 X. L. Wang, J. Y. Zhang, Z. H. Chang, Z. Zhang, X. Wang, H. Y. Lin and Z. W. Cui, α–γ-Type $[Mo_8O_{26}]^{4-}$-Containing Metal–Organic Complex Possessing Efficient Catalytic Activity toward the Oxidation of Thioether Derivatives, *Inorg. Chem.*, 2021, **60**, 3331–3337.

33 H. Li, P. He, R. Wan, Y. Zou, X. Zhao, P. Ma, J. Niu and J. Wang, Trinuclear ruthenium core-containing polyoxometalate-based hybrids: preparation, characterization and catalytic behavior, *Dalton Trans.*, 2020, **49**, 2895–2904.

34 J. Y. Zhang, Y. C. Zhang, X. L. Wang, Z. H. Chang, Z. Zhang, H. Y. Lin and Z. W. Cui, Polyoxometalate-based Cu^{II}/Co^{II} complexes tuned using various metal–pyrazole loops: design, diverse architectures and catalytic activity toward the oxidation of thioether derivatives, *CrystEngComm*, 2022, **24**, 3172–3178.

35 Q. Xu, X. Liang, B. Xu, J. Wang, P. He, P. Ma, J. Feng, J. Wang and J. Niu, 36-Nuclearity Organophosphonate-Functionalized

Polyoxomolybdates: Synthesis, Characterization and Selective Catalytic Oxidation of Sulfides, *Chem. Eur. J.*, 2020, **26**, 14896–14902.